Received: 28 September 2021 | Revised: 30 April 2022 | Accepted: 9 May 2022 | Published on: 8 June 2022

DOI: 10.1002/joc.7729

RESEARCH ARTICLE

International Journal of Climatology RMetS

Intercomparisons of methods for extracting the internal climate variability from the observed records over the Indo-Pacific sector

Yuma Miyaji[1] | Takuya Hasegawa[2,3] | Youichi Tanimoto[2]

[1]Graduate School of Environmental Science, Hokkaido University, Sapporo, Japan

[2]Faculty of Environmental Earth Science and Graduate school of Environmental Science, Hokkaido University, Sapporo, Japan

[3]Graduate School of Science, Tohoku University, Sendai, Japan

Correspondence
Yuma Miyaji, Graduate School of Environmental Science, Hokkaido University, N10 W5, Kita-ku, Sapporo, Hokkaido 060-0810, Japan.
Email: miyaji25@ees.hokudai.ac.jp

Funding information
Japan Society for the Promotion of Science, Grant/Award Numbers: JP18H03726, JP19H05702, JP20K04072

Abstract

A careful isolation of the externally forced component (EFC) and the internal climate variability (ICV) embedded in the observed records as well as the climate simulations is critical to investigate an actual response to the external radiative forcing and/or background dynamics in the ICV. Employing three different methods, we evaluate the EFCs contained in the observed sea surface temperature (SST) and sea level pressure (SLP) fields in the Indo-Pacific region. After removing these EFCs, we obtain the respective ICVs as the remaining anomalies. The remaining SST and SLP anomalies are then evaluated on decadal time scales in a combined empirical orthogonal function (EOF) analysis of different spatial portions: the tropical Pacific, the Indian Ocean and the whole Indo-Pacific region. After making statistical intercomparisons of the spatial patterns and associated time series of the EOF analyses, we found that the EFCs of the individual grid point values (GPVs) were appropriately estimated by regressing onto the multi-model ensemble global mean surface temperature ($GMST_{MME}$) and were less well approximated by the conventional linear trend and the multi-model ensemble mean of the simulated GPVs. The regressed SST anomalies of the individual historical simulations onto the $GMST_{MME}$ were much larger than the observed anomalies, illustrating that the ICV-to-EFC variance ratio is a performance-improvement indicator of climate models.

KEYWORDS

cross-basin interaction, decadal, external forcing, Indian Ocean, Interdecadal Pacific Oscillation, internal variability, Pacific, statistical methods

1 | INTRODUCTION

Since the Industrial Revolution, increased anthropogenic greenhouse gases have raised the global mean surface temperature (GMST; Hegerl *et al.*, 2007). The GMST increase accelerated during the 1980s and 1990s but has slowed or paused since 2000 (Easterling and Wehner, 2009). Then, this global warming hiatus is commonly recognized to have ended around 2012 (Medhaug *et al.*, 2017). These decadal modulations in the increase rate of GMST are largely attributed to the internal climate variability (ICV) of the ocean–atmosphere rather than to modulations in radiative forcing (Kosaka and Xie, 2016). Hence, the observed long-term climate variations contain both the ICV and an externally forced component (EFC).

Several studies have linked the slowdown of the global warming trend to increased ocean heat uptake (Meehl *et al.*, 2011; Chen and Tung, 2014). The increased ocean heat uptake over the tropical Pacific (TP) is associated with a transition to the negative phase of the Interdecadal Pacific Oscillation (IPO), which significantly contributes to the slowdown of global warming (Kosaka and Xie, 2013; England *et al.*, 2014). The uptaken heat at the TP has been advected through the Indonesia archipelago and stored in the surface layers of the Indian Ocean (Lee *et al.*, 2015; Maher *et al.*, 2018). Whereas the Pacific climate variability is dominated by ICVs such as the IPO, the long-term climate variability over the Indian Ocean is predominantly affected by external forcing (Han *et al.*, 2014a). Under global warming conditions, the sea surface temperature (SST) over the Indian Ocean has warmed more rapidly than the global average SST (Du and Xie, 2008). This trend has influenced the long-term climate variability over the Pacific by modulating the atmospheric Walker circulation (Luo *et al.*, 2012). Thus, an excess heat exchange between the Pacific and Indian Ocean is found in both the upper ocean and troposphere. Elucidating the background mechanism of this heat exchange is essential for understanding future climate change and its decadal modulation over the Indo-Pacific region.

Based on the existing records, estimating the relative contributions of the external forcing effect and the ICV of the ocean–atmosphere system to the long-term climate variability is a challenging task, because external forcing causes a nonuniform effect on the tropical ocean and is a nonlinear function of the increase rate of external radiative forcing. As the ICV is difficult to extract from the observed records, the trans-basin internal decadal variability between over the Pacific and over the Indian Ocean remains incompletely understood.

Han *et al.* (2014b) attempted to extract the ICV from the observed SST records by removing the linear trends at individual grid points. They found a positive correlation between the IPO index and the decadal SST variability over the Indian Ocean during the early period (1900–1984), but a negative correlation during the latest years (1984–2008). However, Han *et al.* (2014b) did not discuss the primary reasons for the sign change of the correlation. Dong and McPhaden (2017) attempted a different extraction of the ICV from the observed SST records and discussed whether the sign change of the correlation was a truly observed finding or an aliasing artefact caused by inappropriate statistical treatment. After removing the multi-model ensemble mean (MME) of the historical simulations of the Coupled Model Intercomparison Project 5 (CMIP5) from the observed SST records at individual grid points, they found that the IPO index was positively correlated with the decadal SST variability over the Indian Ocean throughout the analysed span (1900–2012).

Assuming that the MME truly represents the nonlinear effect of external forcing at any location, a linear detrending treatment is expected to generate artificial ICV. To discuss the background mechanism of the ICV over the Indo-Pacific region, we require an appropriate statistical analysis of all observed climate variables in the ocean and atmosphere as well as the SST. Although Xu and Hu (2018) removed the EFC from the simulated SST in long-term ocean–atmosphere coupled model simulations, ways of removing the EFC from the observed records of the SST and other climate variables are unexplored. To bridge this gap, the present study compares the results of different procedures in EFC estimation and seeks the most appropriate procedure for estimating the decadal ICV over the Indo-Pacific sector from the observed records.

The remainder of this paper is organized as follows. Section 2 describes the data and methods for obtaining the internal variability. Section 3 compares the ICVs over the Indo-Pacific sector extracted from the observed records by different methods. In section 4, we discuss the discrepancies between the ICVs of the observed records and of the historical simulations. Our findings are summarized in section 5.

2 | METHODS

2.1 | Observations

The observation data were three pairs of monthly SSTs and sea level pressures (SLPs) collected from 1958 to 2017 inclusive. These pairs are referred to as (a) Japanese Reanalysis (JRA), (b) the National Center for Environmental Prediction (NCEP) and (c) the European Re-Analysis (ERA) project (see Table 1). The SLP data were extracted from atmospheric reanalysis datasets and the SST data were the lower boundary conditions of these reanalysis datasets (see references in Table 1). To lengthen the records, we combined the global (sea) Ice and SST (GISST) and Optimum Interpolation SST (OISST) as consecutive SST records for the NCEP SST. Similarly, we combined the ERA-40 and ERA-Interim data as the ERA SLPs. To avoid atmospheric variability

TABLE 1 Datasets of observed SST and SLP

	Variable	Dataset	Period	Resolution (latitude × longitude)
JRA	SST	COBE-SST 2 (Hirahara *et al*., 2014)	1958–2017	1° × 1°
	SLP	JRA-55 (Kobayashi *et al*., 2015)	1958–2017	1.25° × 1.25°
NCEP	SST	GISST 2.3b (Rayner *et al*., 1996)	1958–1981	1° × 1°
		OISST v2 (Reynolds *et al*., 2007)	1982–2017	0.25° × 0.25°
	SLP	NCEP/NCAR Reanalysis 1 (Kalnay *et al*., 1996)	1958–2017	2.5° × 2.5°
ERA	SST	HadISST 1 (Rayner *et al*., 2003)	1958–1978	1° × 1°
		ERA-Interim (Dee *et al*., 2011)	1979–2017	0.75° × 0.75°
	SLP	ERA-40 (Uppala *et al*., 2005)	1958–1978	2.5° × 2.5°
		ERA-Interim	1979–2017	0.75° × 0.75°

TABLE 2 CMIP5 models and numbers of ensemble members used in this study

Model name	Historical	RCP4.5
CanESM2	3	3
CCSM4	3	3
CNRM-CM5	3	1
CSIRO-Mk3L-1-2	3	3
GFDL-CM3	3	3
GISS-E2-H	3	3
HadGEM2-ES	3	3
IPSL-CM5A-LR	3	3
MIROC5	3	3
MPI-ESM-LR	3	3
MRI-CGCM3	3	1
NorESM1-M	3	1

over the land, we analysed only the SLP data over the ocean. To standardize the different spatial resolutions of the individual datasets, all SST and SLP data were regridded at a horizontal resolution of 2° longitude × 2° latitude by using bilinear interpolation. Monthly anomalies were obtained by removing the monthly climatologies averaged over the 1958–2017 period from the original monthly records and then passing those monthly anomalies through an 8-year lowpass filter to extract the decadal variations.

Each of the SST datasets was reconstructed from different instrumental measurements using different spatial-smoothing and temporal-interpolation methods (Yasunaka and Hanawa, 2011). Likewise, each of the atmospheric reanalysis datasets was produced by assimilating different observations with different numerical models (Zhang *et al*., 2016). Thus, the individual datasets may include systematic errors in the 50-year records. To obtain the common features of the long-term signals in those datasets, we merged the three SST (SLP) datasets into a virtually single SST (SLP) field for the EOF analysis. The EOF analysis (see section 2.3 for details) provided the solid observed evidence that is independent of the dataset selection.

2.2 | Multi-model data

We utilized multi-model climate simulations in the CMIP5 (Taylor *et al*., 2012) to evaluate the EFC contained in the observed datasets. We employed the SST, SLP and surface air temperature (SAT) data of 1958–2005 for the historical runs and the RCP4.5 runs for 2006–2017. Following the previous studies (Dong and Mcphaden, 2017), the RCP4.5 runs were selected among several runs of future projection because the number of the climate models with ensemble members was largest under the RCP4.5 scenario than in other scenarios. We thus selected 12 climate models with three ensemble members (see Table 2) to suppress the ICVs in the MMEs that were calculated from 36 and 30 simulations over the 1958–2005 and 2006–2017 periods, respectively. Note that the scenario selection is unlikely to affect the following results because the GMST spread among the future projections of different scenarios was reasonably small during the 2006–2017 period.

As described for the observations, the simulated GPVs were regridded onto a horizontal resolution of 2° longitude × 2° latitude and passed through an 8-year lowpass filter.

2.3 | Method

Long-term observed records of ocean and atmospheric variables tend to contain both ICVs in the ocean–atmosphere system and EFCs introduced by anthropogenic and natural radiative forcing. To investigate the remote effect of the internal IPO on the climate variations in other tropical basins, the ICV must be accurately extracted from the observed records by isolating the EFC. In most of the previous studies, a linear trend estimated by the least-squares method was removed from the observed record, and the remaining signal was treated as the ICV. This linear detrending method is easy and simple, but whether the ICVs are properly represented in the linearly detrended signal is doubtful. As introduced in the previous section, Dong and McPhaden (2017) report that a 21-year running window correlation of the decadal SST variability between the Indian and Pacific Ocean undergoes a dramatic transformation around 1985 with a change in the sign, when the linear detrend is applied in isolating the ICVs. Meanwhile this interbasin correlation shows the sustained sign over several decades when the ICVs are calculated by removing the MME of the historical simulations from the observed records.

Based on observations, we here investigate the cross-basin relationship of the decadal SST variability between over the Indian Ocean and over the TP. To discuss the likely background mechanism of the cross-basin relationship, we statistically analysed the observed records and attempted to accurately obtain the ICV of both the SST records and the other ocean and atmosphere variables.

In later sections, we perform an intercomparison of three methods (Methods I, II, and III) and estimate the EFC of each variable. Method I utilizes the MME of GMST ($\mathrm{GMST_{MME}}$) as a representative index of the EFC (see next paragraph for details). Method II applies the conventional detrending method to each variable at each grid point. In Method III, first we calculate the MME time series of each variable at each grid point based on the selected 36 simulations. The ICVs are expected to be suppressed in that MME time series because the ICVs among individual simulations tend to be temporally uncorrelated. Thus, we remove these MME time series from the observed records at the same grid points in order to extract the ICVs in the observed records. Method III follows Dong and McPhaden (2017) but is here extended to all variables (not the SST alone).

Method I assumes that the EFC of each variable at each grid point is synchronized with the time series of the $\mathrm{GMST_{MME}}$. In Dai *et al.* (2015), this assumption is applied only to the SAT, but is here applied to all climate variables.

Let t be time steps and e be assigned numbers of simulated ensemble members. $\mathrm{GMST_{MME}}$ (t) is calculated from 36 GMST (t, e) as

$$\mathrm{GMST_{MME}}(t) = \frac{1}{36}\sum_{\mathrm{e}=1}^{36}\mathrm{GMST}(t,e). \tag{1}$$

where GMST(t,e) is time series of an area-average of SAT over the globe in the individual ensemble members. Since the ICVs in 36 time series of GMST are assumed to be uncorrelated each other, the $\mathrm{GMST_{MME}}(t)$ is expected to reflect only the external forcing. Therefore, the EFC of the observed variable at each grid point i can be calculated as

$$X_{\mathrm{EFC}}(t,i) = \alpha_X(i)\times\mathrm{GMST_{MME}}(t)+\beta(i), \tag{2}$$

where $X_{\mathrm{EFC}}(t,\ i)$ is the EFC of observed variable $X(t,\ i)$, $\alpha_X(t,\ i)$ is the regression coefficient of the observed X onto the $\mathrm{GMST_{MME}}$, and $\beta(i)$ denotes the constant residuals. Consequently, the ICV (X_{ICV}) is determined as

$$X_{\mathrm{ICV}}(t,i) = X(t,i) - X_{\mathrm{EFC}}(t,i). \tag{3}$$

Given a large number of the ensemble members as in Watanabe *et al.* (2021) who employed 220 members in total based on a combined set of large ensembles only from four different climate models, the EFC of each variable at each grid point is most appropriately evaluated by Method III. In contrast, Method I is expected to properly remove the ICV from the GMST time series because it performs spatial averaging over the globe and also averages over the 36 simulations, thus suppressing the ICV in the surface temperature time series.

We further compared Methods I, II and III against an analysis of nonextracted anomalies that retains both the EFC and ICV (Method IV).

2.4 | Combined EOF analysis

Let N be the number of grid points over the target analysis domain (e.g., the TP) and T be the number of time steps. Expressing the SST anomalies in the individual dataset as $x(t,\ n)$, the covariance $v(n1, n2)$ between locations $n1$ and $n2$ is calculated as follows:

$$v(n1,n2) = \frac{1}{T-1}\sum_{t=1}^{T}x(t,n1)x(t,n2). \tag{4}$$

Recall that the SST anomalies from the three SST datasets (JRA, NCEP and ERA) are combined into a single EOF analysis by concatenating in space. Hence, the $3N\times 3N$ covariance matrix of this combined EOF analysis is given by

$$V = \begin{bmatrix} v(1,1) & \cdots & v(1,3N) \\ \vdots & \ddots & \vdots \\ v(3N,1) & \dots & v(3N,3N) \end{bmatrix}, \\ = \begin{bmatrix} V_{\text{JRA,JRA}} & V_{\text{JRA,NCEP}} & V_{\text{JRA,ERA}} \\ V_{\text{NCEP,JRA}} & V_{\text{NCEP,NCEP}} & V_{\text{NCEP,ERA}} \\ V_{\text{ERA,JRA}} & V_{\text{ERA,NCEP}} & V_{\text{ERA,ERA}} \end{bmatrix}. \quad (5)$$

For example, $V_{\text{JRA,JRA}}$ and $V_{\text{NCEP,JRA}}$ are described by Equations (6) and (7), respectively,

$$V_{\text{JRA,JRA}} = \begin{bmatrix} v(1,1) & \dots & v(1,N) \\ \vdots & \ddots & \vdots \\ v(N,1) & \cdots & v(N,N) \end{bmatrix}, \quad (6)$$

$$V_{\text{NCEP,JRA}} = \begin{bmatrix} v(N+1,1) & \dots & v(N+1,N) \\ \vdots & \ddots & \vdots \\ v(2N,1) & \dots & v(2N,N) \end{bmatrix}. \quad (7)$$

Here, $V_{\text{JRA,JRA}}$, $V_{\text{NCEP,NCEP}}$ and $V_{\text{ERA,ERA}}$ are the $N \times N$ covariance matrices calculated from the JRA, NCEP and ERA SSTs, respectively. The individual elements in the covariance matrices were calculated from $x(t, n)$ in the same datasets, as done in the conventional EOF analysis. Meanwhile, the matrix elements in $V_{\text{JRA,NCEP}}$, $V_{\text{JRA,ERA}}$ and $V_{\text{NCEP,ERA}}$ and their transposed elements in V are calculated from the $x(t, n)$ of the different datasets. If the SST anomalies of the different datasets are correlated, the leading modes of the matrix V in the combined EOF analysis are expected to emphasize the common signals of decadal climate variability among the datasets.

The combined EOF analysis of these three SST datasets obtains the single principal component of the leading mode with T steps (SST PC1) from the covariance matrix V. The associated spatial loadings of the leading mode (hereafter denoted by EOF1) are the regressed SST anomalies onto the SST PC1. The regression pattern is presented as the average of the regression patterns of the three individual datasets.

Applying this combined EOF analysis to the remaining SST anomalies extracted by Methods I–IV, we obtained four types of SST PC1s and their associated SST EOF1s.

Applying the same analysis to the remaining SLP anomalies extracted by Methods I–IV, we also obtained four types of SLP PC1 and their associated SLP EOF1s.

In addition to the above combined EOF analysis by concatenating in space (S-EOF analysis), we also applied an alternative combined EOF analysis by concatenating in time (T-EOF analysis), following Neeti and Eastman (2014). In the T-EOF analysis, we obtain the PC1 with $3 \times$ T steps from the $N \times N$ covariance matrix. Therefore, after separating into the three single PC1s with T steps, those three PC1s are averaged. The PC1 from the S-EOF analysis and the one from the T-EOF analysis are highly correlated each other, for any variable of SST or SLP in any domain, as well as in any Methods I–IV. This means that we will reach the same conclusion, no matter which method we choose, S-EOF analysis or T-EOF analysis. For simplicity, we will present the results with S-EOF analysis in later sections.

In the next section we will present temporal correlation coefficients (TCCs) among time series of PC1s, as well as spatial correlation coefficients (SCCs) among spatial pattern of EOF1s. To test significances of those correlation coefficients, we performed a two-tailed significance test based on the Student's t distribution with eight degrees of freedom. Significant correlation coefficients at 95% confidence level are shown with asterisks in Figures 1–6 and Tables 3–8.

3 | COMPARISONS OF METHODS

3.1 | Individual domains

The combined EOF analyses of Methods I–IV were applied to the remaining anomalies over three domains of the SST field: the TP (120°E–80°W, 20°S–20°N), the tropical Indian Ocean (TIO; 40°–110°E, 20°S–20°N), and the whole Indo-Pacific sector (WIP; 40°E–80°W, 60°S–60°N). The same procedure was applied to the remaining SLP anomalies. Finally, we obtained 12 leading EOFs and their accompanying PCs for the SST field, along with 12 sets of EOFs and PCs for the SLP field. To simplify the analysis, we represent the EOF1s and PC1s of the remaining SST anomalies as ${}^{\text{Method}}\text{EOF1}^{\text{domain\_SST}}$ and ${}^{\text{Method}}\text{PC1}^{\text{domain\_SST}}$, respectively. For example, the EOF1 and PC1 of Method I in the TP domain are represented by ${}^{\text{I}}\text{EOF1}^{\text{TP\_SST}}$ and ${}^{\text{I}}\text{PC1}^{\text{TP\_SST}}$, respectively.

In the present study, the TP rather than the whole Pacific was selected as an analysis domain because the climate variabilities over the Pacific and Indian Ocean are coupled over the Tropics (Chikamoto *et al.*, 2015). The TIO domain was adopted for the same reason. However, in an EOF analysis over the whole Pacific, the intercomparison among Methods I–IV led to the same conclusions as the TP analysis (data not shown).

Tropical Pacific

Figure 1 shows the patterns of the leading EOFs of the TP obtained by Methods I–IV, namely ${}^{\text{I}}\text{EOF1}^{\text{TP\_SST}}$,

${}^{\mathrm{II}}\mathrm{EOF1}^{\mathrm{TP\_SST}}$, ${}^{\mathrm{III}}\mathrm{EOF1}^{\mathrm{TP\_SST}}$ and ${}^{\mathrm{IV}}\mathrm{EOF1}^{\mathrm{TP\_SST}}$, along with their accompanying time series of ${}^{\mathrm{I}}\mathrm{PC1}^{\mathrm{TP\_SST}}$, ${}^{\mathrm{II}}\mathrm{PC1}^{\mathrm{TP\_SST}}$, ${}^{\mathrm{III}}\mathrm{PC1}^{\mathrm{TP\_SST}}$ and ${}^{\mathrm{IV}}\mathrm{PC1}^{\mathrm{TP\_SST}}$. An individual PC1 in Figure 1 is calculated by projecting SST anomalies of the three datasets at a particular time onto the EOF1 obtained from the combined EOF analysis for SST anomalies over the TP domain. Then, onto this PC1, we can calculate regressed SST anomalies over the whole Indo-Pacific sector rather than only over the TP domain. Since those regressed SST anomalies are obtained for the three datasets, the average of the three regressed anomalies at a particular grid point is plotted as the spatial pattern as in the left panels in Figure 1. In all spatial pattern in the later figures, the averages of the three regressions are plotted.

The regressed spatial pattern of ${}^{\mathrm{I}}\mathrm{EOF1}^{\mathrm{TP\_SST}}$ shows basin-wide positive anomalies in the TP, along with negative anomalies over the mid-latitudes in the North and South Pacific (Figure 1a). This tripole pattern of SST anomalies over the whole Pacific was characterized as an

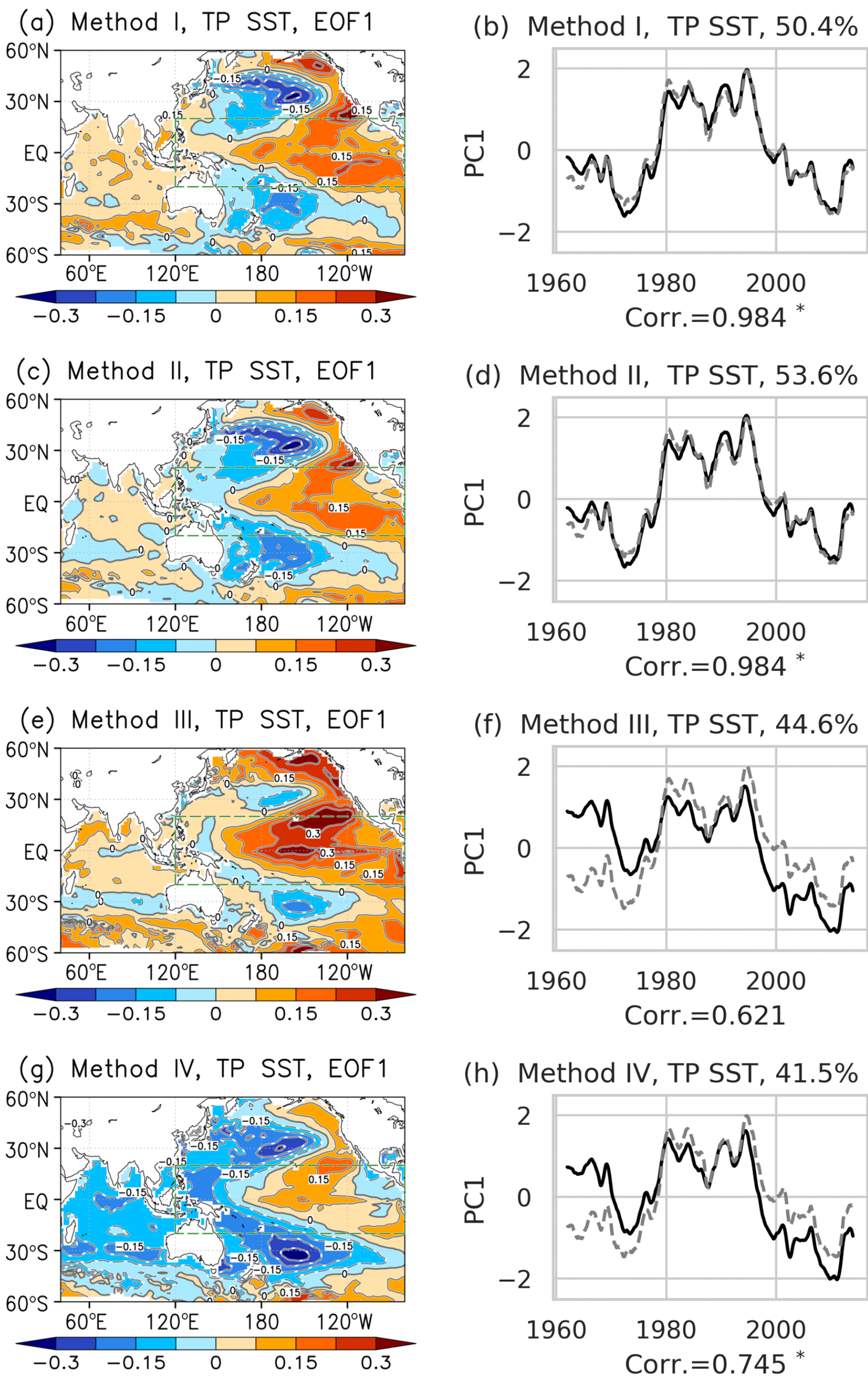

FIGURE 1 Regressed anomalies of EOF1 (left panels) and time series of PC1 (right panels) in the combined EOF analysis of SST (in K) across the three datasets over the tropical Pacific (TP, 120°E–80°W, 20°S–20°N). Rows show the internal variabilities extracted by Methods I–IV. The contour interval is 0.075 K and positive (negative) values are represented by solid (dashed) lines in the left panels. Grey dashed lines in the right panels denote the SLP PC1s over the TP obtained by the same method. All time series are standardized. The top right and bottom centre of each panel state the percentage of the explained variance and the temporal correlation coefficients between the SST PC1 and the SLP PC1, respectively. The correlation coefficients with asterisks are statistically significant at 95% confidence level with eight degrees of freedom by 2-tailed test based on the Student's *t* distribution. The boxes (dashed line) in the left panels enclose the TP domain [Colour figure can be viewed at wileyonlinelibrary.com]

IPO-like pattern in previous studies (Power *et al.*, 1999; England *et al.*, 2014), although the latitude range of the TP domain in our EOF analysis is narrower than in the earlier studies. Besides, slight positive SST anomalies were widespread over the Tropics and subtropics of the Indian Ocean. The temporal evolution of $^{I}PC1^{TP\_SST}$ (Figure 1b) depicts a negative-to-positive phase transition in the late 1970s and an opposite transition in the late 1990s. Decadal variations such as the climate-regime shift over the Pacific in 1976/1977 (Nitta and Yamada, 1989; Trenberth and Hurrell, 1994; Deser and Phillips, 2006) and the persistent negative phase of the IPO after 2000 (Henley, 2017) also appeared in the time series.

The decadal SST variations were associated with pronounced decadal SLP variations all over the Pacific. The regressed spatial pattern of $^{I}EOF1^{TP\_SLP}$ (Figure 2a) appeared as a zonal seesaw over the TP with a positive (negative) centre in the west (east), along with negative anomalies in the North and South Pacific with a centre of action in the mid-latitudes. The decadal variations in the

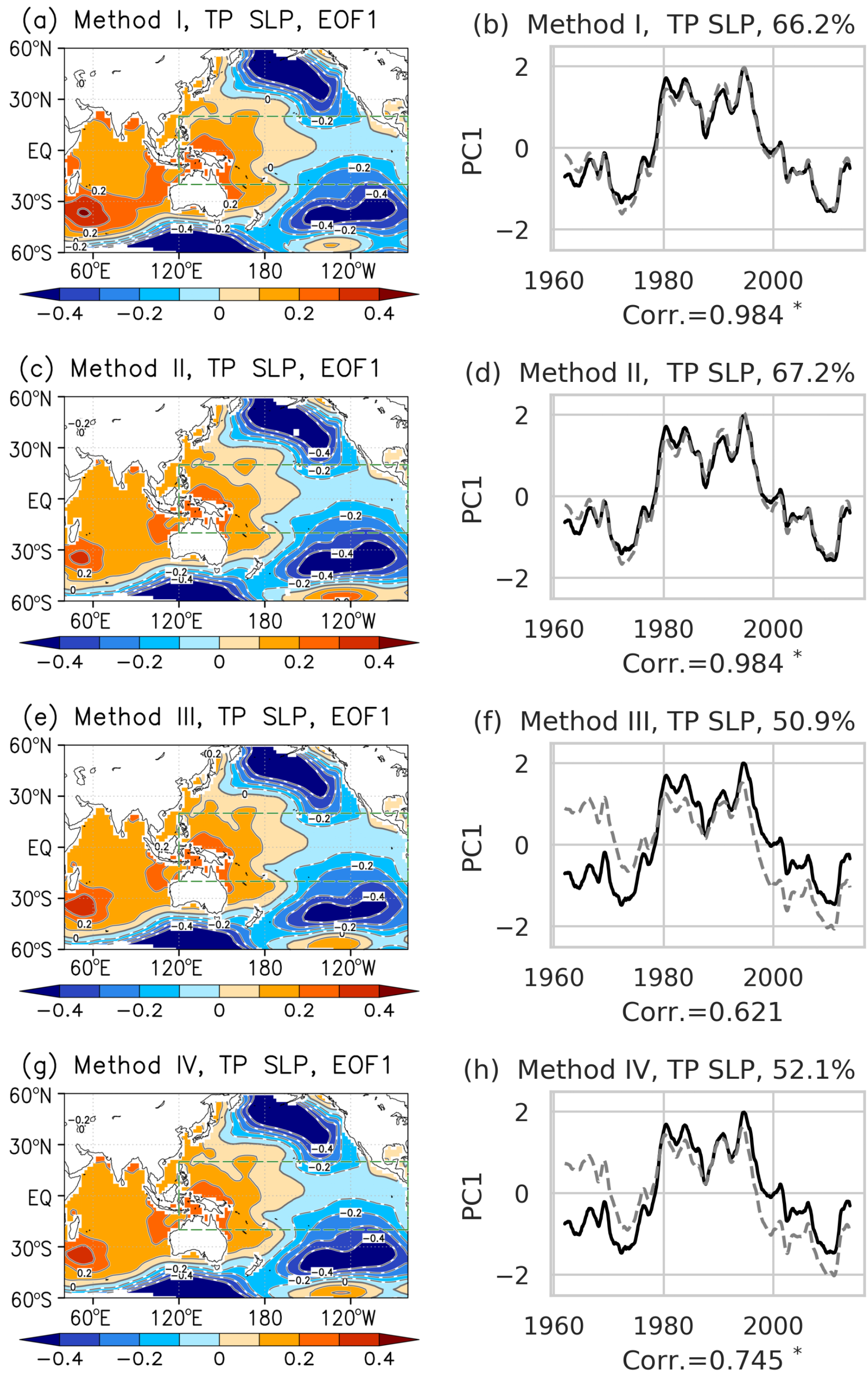

FIGURE 2 As for Figure 1 but showing the SLP (in hPa) over the tropical Pacific (TP; 120°E–80°W, 20°S–20°N). The contour interval is 0.1 hPa and positive (negative) values are represented by solid (dashed) lines in the left panels. Grey dashed lines in the right panels denote the SST PC1s over the TP obtained by the same method [Colour figure can be viewed at wileyonlinelibrary.com]

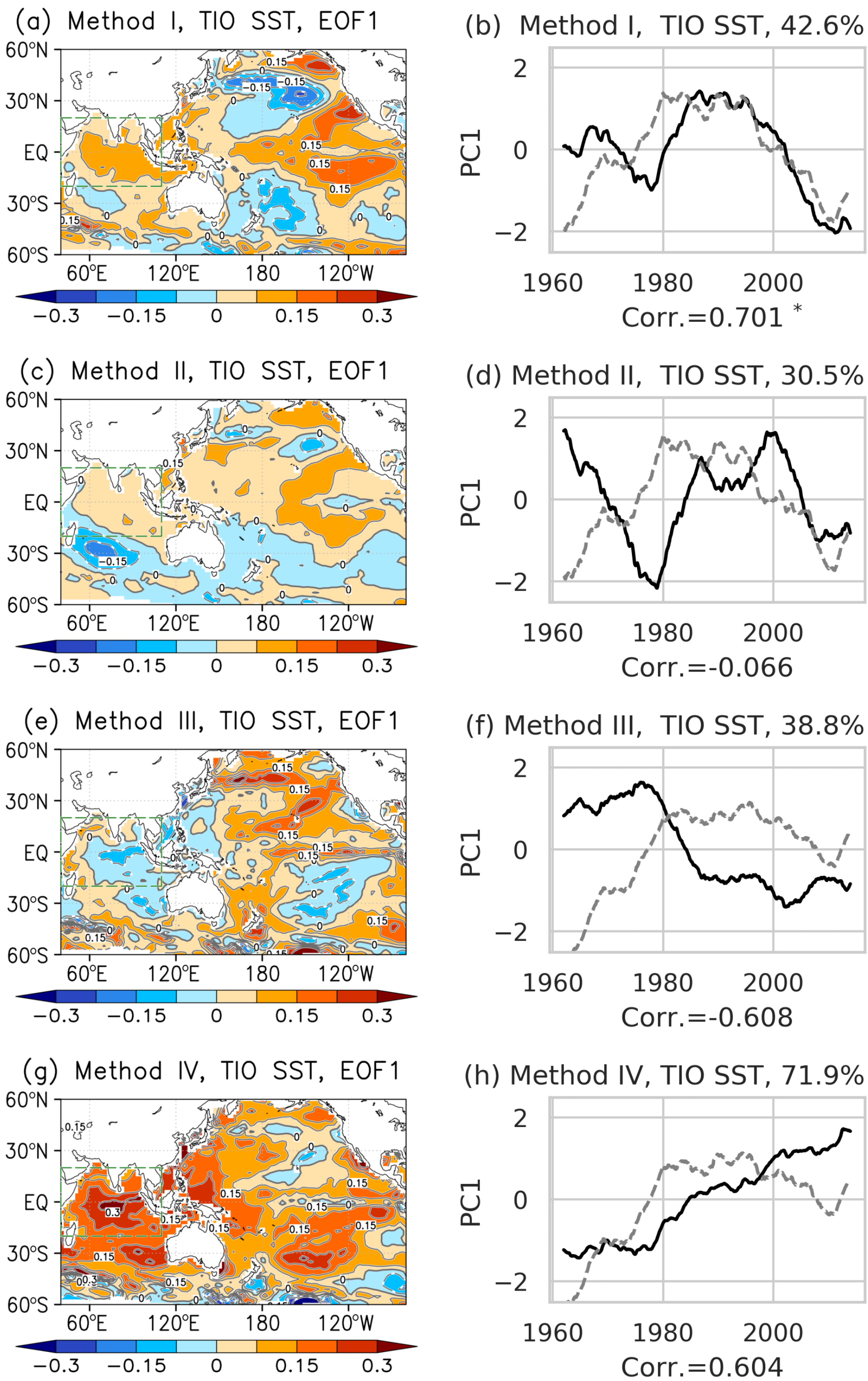

FIGURE 3 As for Figure 1 but showing the SST (in K) over the tropical Indian Ocean (TIO; 40°–110°E, 20°S–20°N). Grey dashed lines in the right panels denote the SST PC1s over the TIO obtained by the same method. The boxes (dashed line) in the left panels enclose the TIO domain [Colour figure can be viewed at wileyonlinelibrary.com]

temporal evolution of $^{I}PC1^{TP\_SLP}$ (Figure 2b) were similar to those in the temporal evolution of $^{I}PC1^{TP\_SST}$.

As revealed in many previous studies, the decadal SST and SLP anomalies over the TP interact through Bjerknes feedback (Bjerknes, 1969; Bordbar *et al.*, 2017). As feedback theory has proven valid and dominant in reality, the dominant internal variabilities of the observed SST and SLP should be significantly correlated. Indeed, the TCC between $^{I}PC1^{TP\_SST}$ and $^{I}PC1^{TP\_SLP}$ was statistically significant (0.984; Figures 1b and 2b). In the spatial patterns of $^{I}EOF1^{TP\_SST}$ and $^{I}EOF1^{TP\_SLP}$, a zonal SST gradient and a zonal SLP seesaw involved in Bjerknes feedback appeared over the TP. Those SST and SLP spatial patterns in the $^{I}EOF1^{TP\_SST}$ and $^{I}EOF1^{TP\_SLP}$ typify Bjerknes feedback in which weakened (enhanced) easterly trade winds associated with a decreased (increased) zonal gradient of SLP over the equatorial Pacific relax (enhance) the zonal SST gradient over the TP. These gradient changes are fed back to the original SLP gradient (L'Heureux *et al.*, 2013; Bordbar *et al.*, 2017).

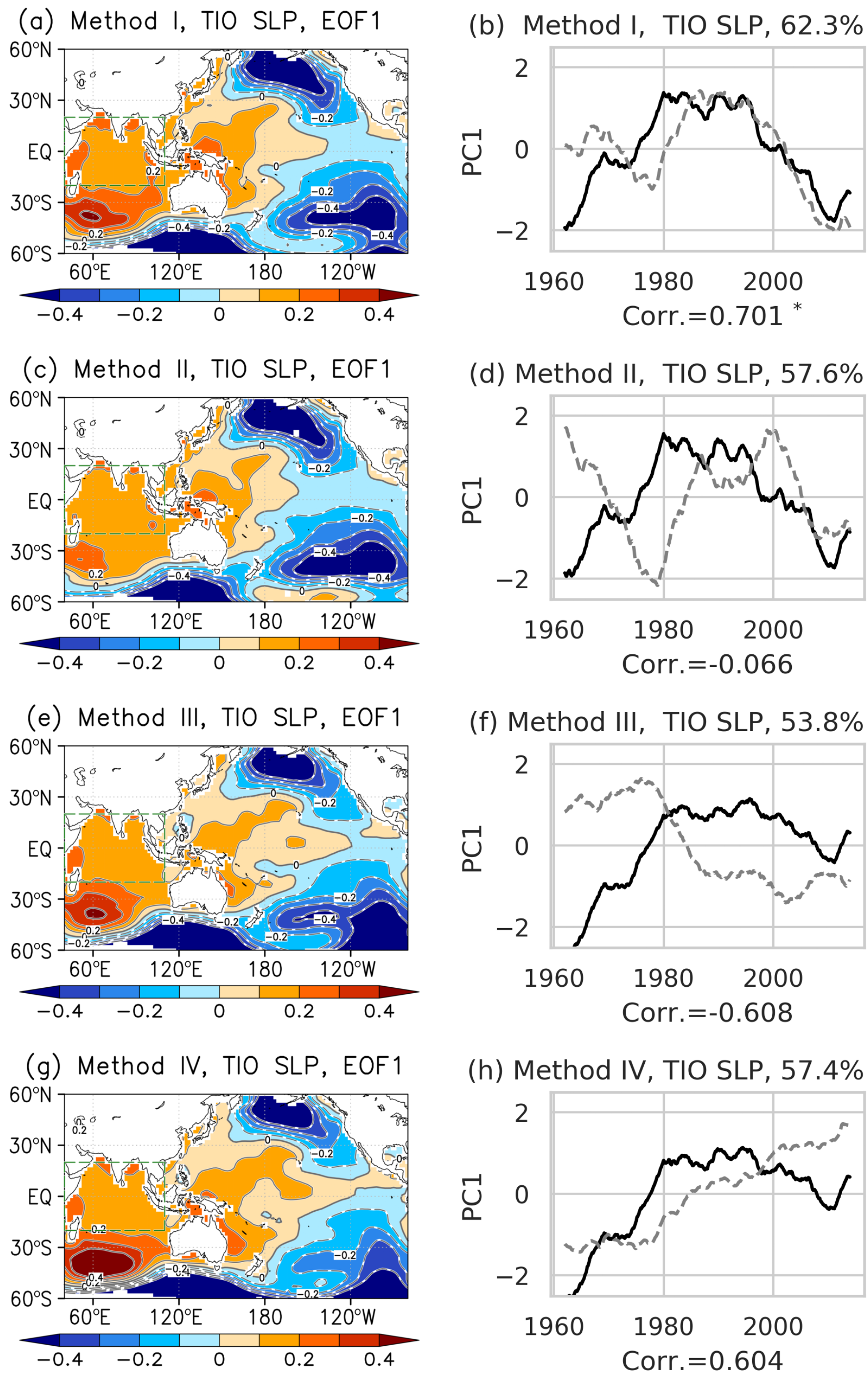

FIGURE 4 As for Figure 1 but showing the SLP (in hPa) over the tropical Indian Ocean (TIO; 40°–110°E, 20°S–20°N). Grey dashed lines in the right panels denote SST PC1s over the TIO obtained by same method. The boxes (dashed line) in the left panels enclose the TIO domain [Colour figure can be viewed at wileyonlinelibrary.com]

The large-scale anomalies in SST and SLP over the TP are accompanied by extratropical anomalies (see Figures 1a and 2a). Over mid-latitudes in the North Pacific, the negative (positive) SLP anomalies with a centre of action around the Aleutian low enhance (weaken) the westerly surface winds. Negative (positive) SST anomalies in the central North Pacific then arise through the increased (decreased) upward surface heat fluxes and southward Ekman advection (Tanimoto *et al.*, 1997; Alexander *et al.*, 2002). The same anomalies occur at mid-latitudes of the South Pacific (Shakun and Shaman, 2009), albeit with weaker amplitudes than in the North Pacific. Hence, the spatial patterns of $^{\mathrm{I}}\mathrm{EOF1}^{\mathrm{TP\_SST}}$ and $^{\mathrm{I}}\mathrm{EOF1}^{\mathrm{TP\_SLP}}$ are temporally related. This inference is corroborated by the similarities of $^{\mathrm{I}}\mathrm{PC1}^{\mathrm{TP\_SST}}$ and $^{\mathrm{I}}\mathrm{PC1}^{\mathrm{TP\_SLP}}$. The relationship between these patterns can be physically interpreted in both the TP and the extratropical Pacific, as discussed in the aforementioned studies.

The spatial patterns of $^{\mathrm{II}}\mathrm{EOF1}^{\mathrm{TP\_SST}}$ and $^{\mathrm{II}}\mathrm{EOF1}^{\mathrm{TP\_SLP}}$ (Figures 1c and 2c, respectively) and the time series of

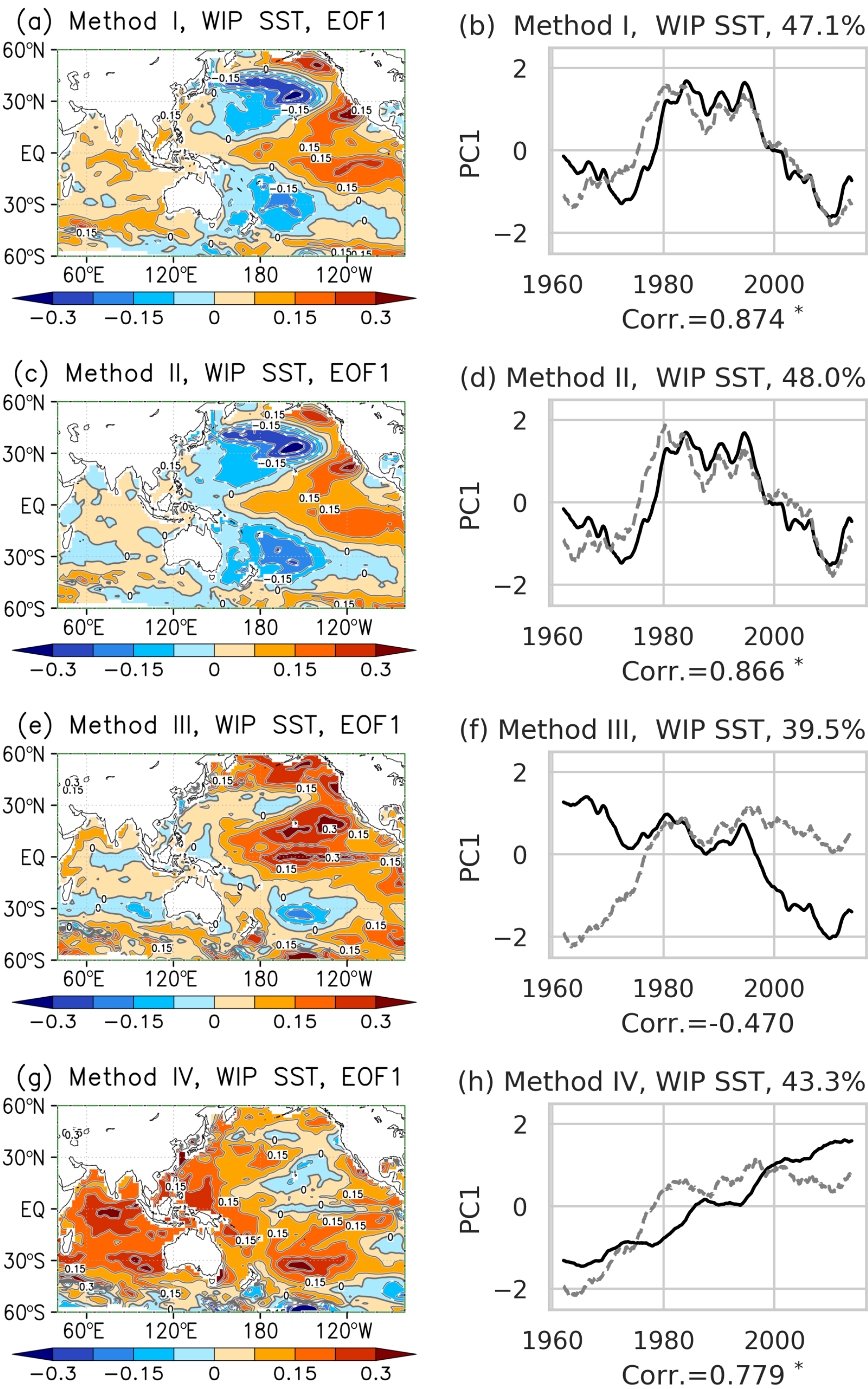

FIGURE 5 As for Figure 1 but showing the SST (in K) over the whole Indo-Pacific sector (WIP; 40°E–80°W, 60°S–60°N). Grey dashed lines in the right panels denote the SST PC1s over the WIP obtained by the same method. The boxes (dashed line) in the left panels enclose the WIP domain [Colour figure can be viewed at wileyonlinelibrary.com]

${}^{II}PC1^{TP\_SST}$ and ${}^{II}PC1^{TP\_SLP}$ (Figures 1d and 2d, respectively) obtained by Method II were similar to those of Method I, implying that ${}^{II}PC1^{TP\_SST}$ and ${}^{II}PC1^{TP\_SLP}$ are significantly correlated (TCC = 0.984). Therefore, Methods I and II obtain the same relationship between the SST and SLP patterns.

After applying Method III, the spatial pattern of ${}^{III}EOF1^{TP\_SLP}$ (Figure 2e) and its associated time series of ${}^{III}PC1^{TP\_SLP}$ (Figure 2f) were similar to those of Methods I and II. However, along the time series of ${}^{III}PC1^{TP\_SST}$ (Figure 1f), positive values appeared during the 1960s and weak negative values appeared during the 1970s. The 2000–2017 period was marked by strong negative values. These features differed from those of ${}^{I}PC1^{TP\_SST}$ and ${}^{II}PC1^{TP\_SST}$ and led to a smaller TCC between ${}^{III}PC1^{TP\_SST}$ and ${}^{III}PC1^{TP\_SLP}$ (0.621) than in Methods I and II.

The four types of EOFs obtained by Methods I–IV give visually identical fields of SST (Figure 1a,c,e,g) and SLP (Figure 2a,c,e,g). However, while the interdecadal

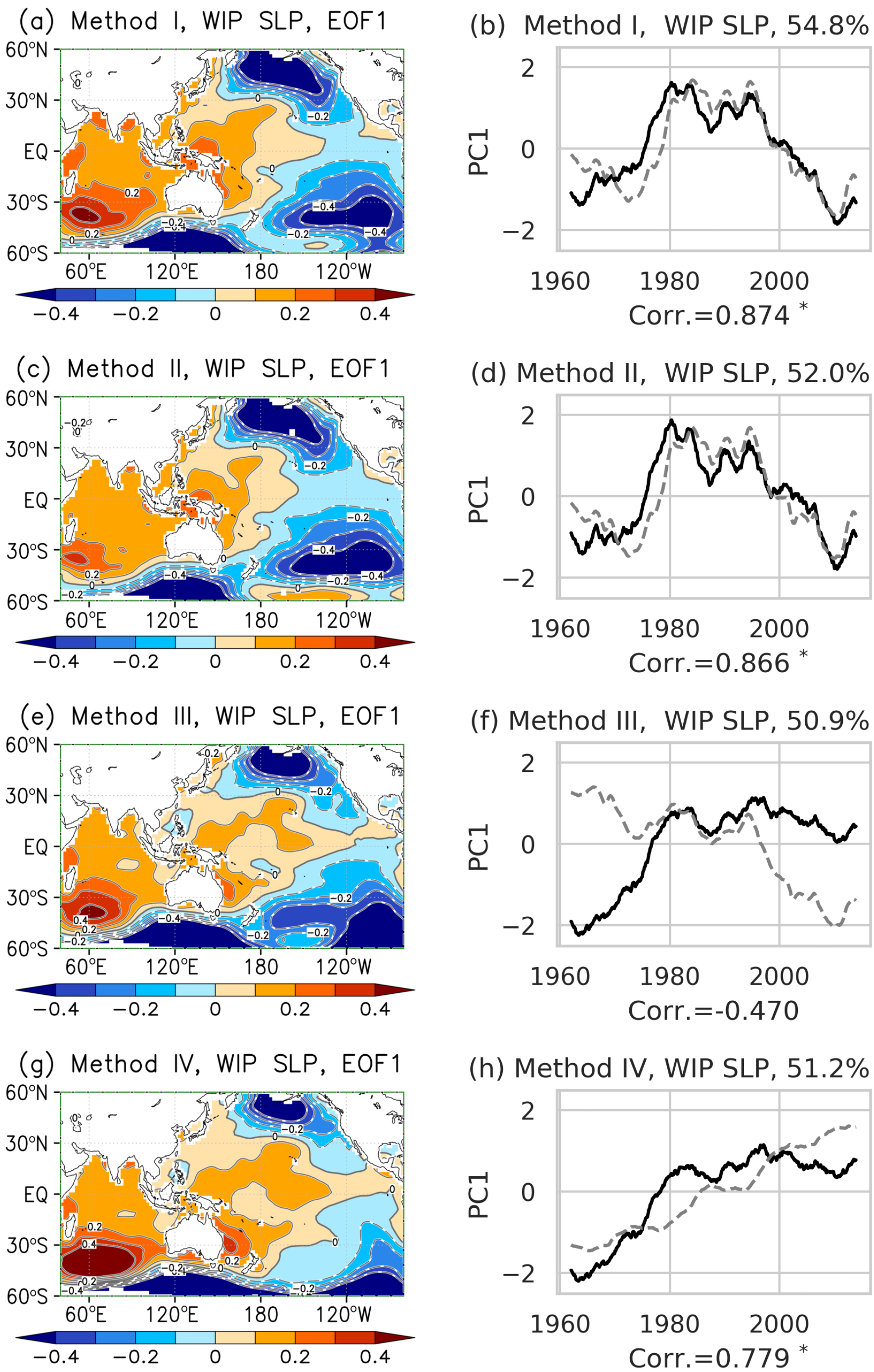

FIGURE 6 As for Figure 1 but showing the SLP (in hPa) over the whole Indo-Pacific sector (WIP; 40°E–80°W, 60°S–60°N). Grey dashed lines in the right panels denote the SST PC1s over the WIP obtained by the same method. The boxes (dashed line) in the left panels enclose the WIP domain [Colour figure can be viewed at wileyonlinelibrary.com]

variations in the time series of the PCs obtained by Methods I and II show correlations between the SST and SLP anomalies (Figures 1b,d and 2b,d), the distinctly descending trend in the SST time series obtained by Method III (Figure 1f) was also obtained by Method IV (Figure 1h), which retained the EFC. These results indicate that Method III does not actually isolate the EFC.

Tropical Indian Ocean

The analytical procedures of Methods I–IV were repeated in the TIO domain (see Figures 3 and 4). The regressed spatial pattern of ${}^{I}\mathrm{EOF1}^{\mathrm{TIO\_SST}}$ (Figure 3a) shows positive anomalies over the entire TIO, along with the typical tripole pattern of the IPO over the whole Pacific (also found in $\mathrm{EOF1}^{\mathrm{TP\_SST}}$; see Figure 1a). The time series of ${}^{I}\mathrm{PC1}^{\mathrm{TIO\_SST}}$ (Figure 3b) was mainly similar to that of the TP, with limited deviations during the 1960s. Meanwhile, the spatial pattern of ${}^{I}\mathrm{EOF1}^{\mathrm{TIO\_SLP}}$ displays positive anomalies over most of the TIO along with the coherent SLP pattern associated with the IPO (Figure 4a) (also found in ${}^{I}\mathrm{EOF1}^{\mathrm{TP\_SLP}}$; see Figure 2a). The time series of ${}^{I}\mathrm{PC1}^{\mathrm{TIO\_SLP}}$ (Figure 4b) is also similar to that over the TP apart from a limited mismatch during the 1960s. Consequently, the TCC between $^{I}PC1^{TIO\_SST}$ and $^{I}PC1^{TIO\_SLP}$ is significantly positive (0.701).

The regressed pattern of $^{II}EOF1^{TIO\_SST}$ (Figure 3c) obtained by Method II captured the positive anomaly over the TIO, but at weaker amplitude than Method I. Over the Pacific, however, the tripole pattern of the IPO was ambiguous. In the spatial pattern of $^{II}EOF1^{TIO\_SLP}$, the coherent SLP pattern associated with the IPO included a dominant zonal SLP seesaw over the TP (Figure 4c). The corresponding time series of $^{II}PC1^{TIO\_SST}$ (Figure 3d) and $^{II}PC1^{TIO\_SLP}$ (Figure 4d) were uncorrelated (TCC = −0.066). The TCC differences between the Methods I and II (0.701 vs. −0.066) means that the Method I was successful in extracting the ocean–atmosphere coupled variability in the TIO as the leading EOFs, but the Method II failed.

The spatial pattern of $^{III}EOF1^{TIO\_SST}$ depicted negative and positive anomalies over the eastern and western parts of the TIO, respectively, along with basin-wide positive anomalies over the Pacific (Figure 3e). The corresponding time series of $^{III}PC1^{TIO\_SST}$ trended obviously downward (Figure 3f). The spatial pattern of $^{III}EOF1^{TIO\_SLP}$ (Figure 4e) displayed the same features as the spatial patterns of $^{I}EOF1^{TIO\_SLP}$ and $^{II}EOF1^{TIO\_SLP}$, but the time series of $^{III}PC1^{TIO\_SLP}$ (Figure 4f) exhibited an upward trend with a quite weak and short negative phase in the 2000s, inconsistent with the time series of $^{III}PC1^{TIO\_SST}$.

As the EFC was not removed in Method IV, the spatial pattern of $^{IV}EOF1^{TIO\_SST}$ shows the geographical intensities of global SST warming (Figure 3g). Significant positive anomalies over the entire TIO of $^{IV}EOF1^{TIO\_SST}$ and the upward trend in $^{IV}PC1^{TIO\_SST}$ (Figure 3h) indicate that SST warming associated with global warming dominates over the TIO. The $^{IV}PC1^{TIO\_SLP}$ also contained an upward trend, but this trend was superimposed with interdecadal variations (Figure 4h). The similarity between $^{III}PC1^{TIO\_SLP}$ and $^{IV}PC1^{TIO\_SLP}$ indicates that over the TIO, the EFC is less effectively removed from the observed SLP in Method III than in Methods I and II.

The upward trends in $^{IV}PC1^{TIO\_SST}$ (Figure 3h) and $^{IV}PC1^{TIO\_SLP}$ (Figure 4h) meant that both time series were positively correlated (TCC = 0.604). Conversely, the downward trend in $^{III}PC1^{TIO\_SST}$ (Figure 3f) opposed the upward trend in $^{III}PC1^{TIO\_SLP}$ (Figure 4f), resulting in a negative TCC (−0.608) between these time series. Thus, in Methods III and IV, the SST PC1 and SLP PC1 were significantly correlated through the common features in their long-term trends. These results indicate that the EFCs over the TIO were not sufficiently removed by Method III.

Whole Indo-Pacific sector

In the previous sections, we obtained the leading EOFs and corresponding PCs of the remaining SST and SLP anomalies in Methods I–IV over the TP and TIO. We now repeat the EOF analysis over the WIP sector (Figures 5 and 6) which covers the whole study domain.

In the regressed spatial pattern of $^{I}EOF1^{WIP\_SST}$ (Figure 5a), the IPO tripole pattern appeared over the whole Pacific. Positive anomalies appeared over the entire TIO, as observed in both $^{I}EOF1^{TP\_SST}$ (Figure 1a) and $^{I}EOF1^{TIO\_SST}$ (Figure 3a). The SLP fields were also similar among $^{I}EOF1^{WIP\_SLP}$ (Figure 6a), $^{I}EOF1^{TP\_SLP}$ (Figure 2a), and $^{I}EOF1^{TIO\_SLP}$ (Figure 4a). The time series of $^{I}PC1^{WIP\_SST}$ (Figure 5b) and $^{I}PC1^{WIP\_SLP}$ (Figure 6b) were significantly correlated (TCC = 0.874) as observed in the Method I analyses of the individual TP and TIO, although the WIP domain is considerably larger than the TP and TIO domains.

The $^{II}EOF1^{WIP\_SST}$ (Figure 5c) and $^{II}EOF1^{WIP\_SLP}$ (Figure 6c) obtained by Method II displays a coherent IPO pattern over the whole Pacific, and the associated SLP pattern includes a zonal SLP seesaw over the TP along with negative anomalies over the mid-latitudes of the North and South Pacific. These findings are consistent with Method I over the WIP domain. Also consistent with Method I, the behaviours of $^{II}PC1^{WIP\_SST}$ (Figure 5d) and $^{II}PC1^{WIP\_SLP}$ (Figure 6d) were similar and thus the two time series were significantly correlated (TCC = 0.866).

The time series of $^{III}PC1^{WIP\_SST}$ trended obviously downward (Figure 5f) and the decadal oscillation in the IPO signal found in $^{I}PC1^{WIP\_SST}$ and $^{II}PC1^{WIP\_SST}$ was absent here. Although the spatial pattern of $^{III}EOF1^{WIP\_SST}$ hints at the IPO tripole pattern, the amplitudes of the SST anomalies were larger in the TP and smaller in the mid-latitudes of the North and South Pacific (Figure 5e) than $^{I}EOF1^{WIP\_SST}$ and $^{II}EOF1^{WIP\_SST}$. As in the EOF analysis over the TIO, the time series of $^{III}PC1^{WIP\_SLP}$ contained an upward trend (Figure 6f), unlike the $^{I}PC1^{WIP\_SLP}$ and $^{II}PC1^{WIP\_SLP}$. Consequently, the TCC between $^{III}PC1^{WIP\_SST}$ and $^{III}PC1^{WIP\_SLP}$ was negative. However, the result was insignificant (TCC = −0.470).

The spatial pattern of $^{IV}EOF1^{WIP\_SST}$ must contain the effect of global warming (Figure 5g). In contrast to the downward trend in $^{III}PC1^{WIP\_SST}$, the $^{IV}PC1^{WIP\_SST}$ monotonically increased (Figure 5h). How the geographical contrast in SLP responds to global SST warming is debatable (Tokinaga *et al.*, 2012), but our $^{IV}EOF1^{WIP\_SLP}$ (Figure 6g) and $^{IV}PC1^{WIP\_SLP}$ (Figure 6h) were mainly identical to the $^{III}EOF1^{WIP\_SLP}$ and $^{III}PC1^{WIP\_SLP}$ pair.

These intercomparisons between Methods III and IV suggest that Method III is not appropriate for removing the EFC from observed records. The downward trend in $^{III}PC1^{WIP\_SST}$ (Figure 5f) probably comes from over-removal of the EFC. In section 4, we will discuss that over-removal is mainly related to overestimations of the

EFC in the individual historical simulations. The high similarities between ^{III}EOF1^{WIP_SLP} and ^{IV}EOF1^{WIP_SLP} and between ^{III}PC1^{WIP_SLP} and ^{IV}PC1^{WIP_SLP} indicate that the current Method III cannot properly isolate the EFC. An insufficient number of ensemble members in the employed CMIP5 data may lead to a biased ensemble mean that fails to represent the EFC of each variable at each grid point.

3.2 | Cross-domain correlation

3.2.1 | Temporal correlations obtained by Method I

Thus far, we have obtained the SST PC1s in three different domains (the TP, TIO and WIP). Table 3(a) is a matrix of the cross-domain TCCs among the three SST PC1s obtained by Method I. All TCCs are significant and exceed 0.733. Table 3(b) is a similar matrix of cross-domain TCCs of the SLP PC1s obtained by Method I. All values are significant and exceed 0.891. In addition, we calculated the cross-domain TCCs between SST PC1 and SLP PC1 by Method I (Table 3(c)). The diagonal components in Table 3 (c) are the cross-variable TCCs given in Figures 1b, 3b and 5b. The significant positive values in this table are unsurprising if the SST and SLP anomalies extracted by Method I represent the true ICV over each domain. These significant cross-domain TCCs indicate that the dominant SST and SLP variabilities in the TP and TIO are well correlated with each other and are closely related to interbasin air–sea interactions over the WIP.

3.2.2 | Spatial correlations obtained by Method I

In addition to the cross-domain TCCs among the PC1s, we calculated the SCCs among the EOF1s (i.e., the cross-domain SCCs). Table 4(a), (b) are matrices of the cross-domain SCCs among the SST EOF1s and SLP EOF1s, respectively, obtained by Method I. All SCCs were calculated for the regressed anomalies over the WIP sector (plotted in the (a) panels of Figures 1–6), although the individual EOF1s were calculated for the SST or SLP anomalies over the individual domains (TP, TIO or WIP). All values in both matrices of Method I are statistically significant (>0.934 for the SST EOF1s and >0.984 for the SLP EOF1s).

We further compared the spatial patterns of SLP EOF1 (Figures 2a, 4a and 6a) and the regressed SLP anomalies onto the SST PC1s over the three domains (data not shown). In the same way, the spatial patterns of

TABLE 3 Cross-domain temporal correlation coefficients (TCCs) between the time series of (a) SST PC1 and (b) SLP PC1 over the tropical Pacific (TP; 120°E–80°W, 20°S–20°N), the tropical Indian Ocean (TIO; 40°–110°E, 20°S–20°N) and the whole Indo-Pacific sector (WIP; 40°E–80°W, 60°S–60°N) based on the ICVs obtained by Method I. Part (c) lists the cross-variable TCCs between the SST PC1 and SLP PC1

(a) Cross-domain TCCs of SST PC1			
Method I	**TP SST**	**TIO SST**	**WIP SST**
TP SST	1.000*		
TIO SST	0.733*	1.000*	
WIP SST	0.980*	0.805*	1.000*
(b) Cross-domain TCCs of SLP PC1			
Method I	**TP SLP**	**TIO SLP**	**WIP SLP**
TP SLP	1.000*		
TIO SLP	0.891*	1.000*	
WIP SLP	0.900*	0.970*	1.000*
(c) Cross-domain TCCs of SST PC1 vs. SLP PC1			
Method I	**TP SLP**	**TIO SLP**	**WIP SLP**
TP SST	0.984*	0.823*	0.831*
TIO SST	0.720*	0.701*	0.668*
WIP SST	0.975*	0.860*	0.874*

Note: Significance for each TCCs is tested by a 2-tailed test based on the Student's *t* distribution. TCCs with asterisk are statistically significant at 95% confidence level with eight degrees of freedom.

SST EOF1 (Figures 1a, 3a and 5a) and the regressed SST anomalies onto the SLP PC1s over the three domains are compared. As summarized in Table 4(c), (d), all SCCs were statistically significant (>0.894). Together, the TCCs in Table 3 and the SCCs in Table 4 indicate that Method I successfully extracted the dominant ocean–atmosphere coupled internal variability across the Indo-Pacific.

3.2.3 | Cross-domain correlations by the other methods

We additionally compiled matrices of the cross-domain TCCs and cross-domain SCCs in Method II (Tables 5 and 6) and Method III (Tables 7 and 8). Note that these correlation coefficients were not always statistically significant.

3.3 | Advantages of Method I

In Method I, the leading PCs and EOFs of the remaining SST and SLP anomalies over the three domains had significantly positive TCCs and SCCs (Tables 3(a), (b) and 4

TABLE 4 Cross-domain spatial correlation coefficients (SCCs) between the leading patterns of the combined EOF1 of (a) SST and (b) SLP over the TP, TIO, and WIP (see Table 3 caption for details) based on the ICVs obtained by Method I. Part (c) lists the SCCs between the leading pattern of SLP EOF1 and the regressed pattern of SLP onto the SST PC1 and (d) lists the SCCs between the leading pattern of SST EOF1 and the regressed pattern of SST onto the SLP PC1

(a) Cross-domain SCCs of SST EOF1			
Method I	**TP SST**	**TIO SST**	**WIP SST**
TP SST	1.000*		
TIO SST	0.934*	1.000*	
WIP SST	0.996*	0.950*	1.000*
(b) Cross-domain SCCs of SLP EOF1			
Method I	**TP SLP**	**TIO SLP**	**WIP SLP**
TP SLP	1.000*		
TIO SLP	0.984*	1.000*	
WIP SLP	0.987*	0.998*	1.000*
(c) Cross-domain SCCs of SLP EOF1 vs. regressed SLP on SST PC1			
Method I	**TP SLP**	**TIO SLP**	**WIP SLP**
TP SST	0.997*	0.949*	0.998*
TIO SST	0.966*	0.935*	0.978*
WIP SST	0.969*	0.932*	0.981*
(d) Cross-domain SCCs of SST EOF1 vs. regressed SST on SLP PC1			
Method I	**TP SST**	**TIO SST**	**WIP SST**
TP SLP	0.996*	0.948*	0.949*
TIO SLP	0.928*	0.901*	0.894*
WIP SLP	0.997*	0.965*	0.966*

Note: Significance for each TCCs is tested by 2-tailed test based on the Student's t distribution. TCCs with asterisk are statistically significant at 95% confidence level with eight degrees of freedom.

(a), (b)). The cross-variable TCCs and SCCs of the PCs and EOFs by Method I were also significant (Tables 3(c) and 4(c), (d)). The spatial patterns of these SST and SLP EOFs indicate an interbasin interaction over the Indo–Pacific sector (Dong and McPhaden, 2017) or a portion of the trans-basin variability over the whole Tropics (Chikamoto *et al*., 2015), implying that Method I well isolated the EFC and thereafter reliably extracted the ocean–atmosphere ICV from the observed records.

In contrast to these advantages in the Method I, the obtained SST PC1 and the SLP PC1 over the TIO of the Method II are uncorrelated (Figure 3d), implying that the Method II failed to extract the dominant ocean–atmosphere coupled variability. In Method III, as shown

TABLE 5 As for Table 3, but based on the ICVs obtained by Method II

(a) Cross-domain TCCs of SST PC1			
Method II	**TP SST**	**TIO SST**	**WIP SST**
TP SST	1.000*		
TIO SST	0.224	1.000*	
WIP SST	0.980*	0.251	1.000*
(b) Cross-domain TCCs of SLP PC1			
Method II	**TP SLP**	**TIO SLP**	**WIP SLP**
TP SLP	1.000*		
TIO SLP	0.889*	1.000*	
WIP SLP	0.890*	0.954*	1.000*
(c) Cross-domain TCCs of SST PC1 vs. SLP PC1			
Method II	**TP SLP**	**TIO SLP**	**WIP SLP**
TP SST	0.984*	0.820*	0.817*
TIO SST	0.161	−0.066	−0.072
WIP SST	0.981*	0.856*	0.866*

TABLE 6 As for Table 4, but based on the ICVs obtained by Method II

(a) Cross-domain SCCs of SST EOF1			
Method II	**TP SST**	**TIO SST**	**WIP SST**
TP SST	1.000*		
TIO SST	0.459	1.000*	
WIP SST	0.996*	0.443	1.000*
(b) Cross-domain SCCs of SLP EOF1			
Method II	**TP SLP**	**TIO SLP**	**WIP SLP**
TP SLP	1.000*		
TIO SLP	0.979*	1.000*	
WIP SLP	0.982*	0.996*	1.000*
(c) Cross-domain SCCs of SLP EOF1 vs. regressed SLP on SST PC1			
Method II	**TP SLP**	**TIO SLP**	**WIP SLP**
TP SST	0.996*	0.122	0.999*
TIO SST	0.958*	−0.032	0.973*
WIP SST	0.960*	−0.019	0.975*
(d) Cross-domain SCCs of SST EOF1 vs. regressed SST on SLP PC1			
Method II	**TP SST**	**TIO SST**	**WIP SST**
TP SLP	0.996*	0.945*	0.943*
TIO SLP	0.412	0.245	0.244
WIP SLP	0.998*	0.964*	0.963*

TABLE 7 Same as Table 3, but based on the ICVs obtained by Method III

(a) Cross-domain TCCs of SST PC1			
Method III	**TP SST**	**TIO SST**	**WIP SST**
TP SST	1.000*		
TIO SST	0.445	1.000*	
WIP SST	0.922*	0.707*	1.000*
(b) Cross-domain TCCs of SLP PC1			
Method III	**TP SLP**	**TIO SLP**	**WIP SLP**
TP SLP	1.000*		
TIO SLP	0.718*	1.000*	
WIP SLP	0.622	0.962*	1.000*
(c) Cross-domain TCCs of SST PC1 vs. SLP PC1			
Method III	**TP SLP**	**TIO SLP**	**WIP SLP**
TP SST	0.621	−0.043	−0.203
TIO SST	−0.246	−0.608	−0.682*
WIP SST	0.336	−0.315	−0.470

TABLE 8 As for Table 4, but based on the ICVs obtained by Method III

(a) Cross-domain SCCs of SST EOF1			
Method III	**TP SST**	**TIO SST**	**WIP SST**
TP SST	1.000*		
TIO SST	0.531*	1.000*	
WIP SST	0.947*	0.762*	1.000*
(b) Cross-domain SCCs of SLP EOF1			
Method III	**TP SLP**	**TIO SLP**	**WIP SLP**
TP SLP	1.000*		
TIO SLP	0.886*	1.000*	
WIP SLP	0.849*	0.996*	1.000*
(c) Cross-domain SCCs of SLP EOF1 vs. regressed SLP on SST PC1			
Method III	**TP SLP**	**TIO SLP**	**WIP SLP**
TP SST	0.311	−0.580	−0.096
TIO SST	−0.196	−0.858*	−0.564
WIP SST	−0.276	−0.892*	−0.632*
(d) Cross-domain SCCs of SST EOF1 vs. regressed SST on SLP PC1			
Method III	**TP SST**	**TIO SST**	**WIP SST**
TP SLP	0.663*	−0.053	−0.218
TIO SLP	−0.217	−0.759*	−0.839*
WIP SLP	0.405	−0.339	−0.493

in the panels (f) of Figures 1–6, SST PC1s and SLP PC1s over the three analysis domains contained a long-term upward or downward trend. Hence, the TCCs among those PC1s in the Method III are not always statistically significant. These trend-like features indicate that the EFCs are not sufficiently removed by the Method III.

In conclusion, we recognize that Method I is the most appropriate method for extracting the ICV from the observed records over the Indo-Pacific sector.

In the next section, we apply Method I to simulated historical records rather than the observed SST and/or SLP records.

4 | APPLICATION TO MULTI-MODEL HISTORICAL SIMULATIONS

Applying Method I to simulated datasets, we now examine how much the observed ICV and EFC are reproduced in the selected CMIP models. Following Method I, we calculated the regressed SST anomalies α_{SST_M} onto the $GMST_{MME}$ at each grid point from the results of 36 historical simulations as described in section 2. Here, we show the area-averages $[\alpha_{SST\_M}]$ on the eastern TP domain (ETP, 180°–80°W, 10°S–10°N), where a distinct SST variance appeared in the ICV extracted from the observed SST records (Figures 1, 3 and 5).

Figure 7a is a histogram of the individual models' $[\alpha_{SST\_M}]$ averaged over the ETP along with their corresponding $[\alpha_{SST}]$ values based on the observed records (Figure 7a). In most of the models, the calculated $[\alpha_{SST\_M}]$ was much larger than the observed $[\alpha_{SST}]$. Such discrepancies were also found in other regions but were especially pronounced over the ETP (Figure 8).

Figure 7b is a histogram of the TCCs between the simulated decadal SST variability over the ETP and the $GMST_{MME}$. The significant TCCs are unrealistic and thereby responsible for the overestimated $[\alpha_{SST\_M}]$. We should note that each individual historical simulation contributes less than 3% to the MME, thereby invalidating such high TCCs. We can reasonably conclude that most of the models overestimated the EFC over the ETP.

Owing to the larger $[\alpha_{SST\_M}]$ than $[\alpha_{SST}]$, the MME of the simulated variances in the EFC was 6.5 times larger than the observed one (second row of Table 9). Consequently, in our definition of Method I, the MME of the simulated variances in the residual ICVs is one-half that of the observed variances (third row). Therefore, the simulated variance ratio of the weak ICVs to the intense EFCs was only 20% of the observed ratio.

Coats and Karnauskas (2017) revealed that vigorous mean upwelling and poleward divergence of the heat flux

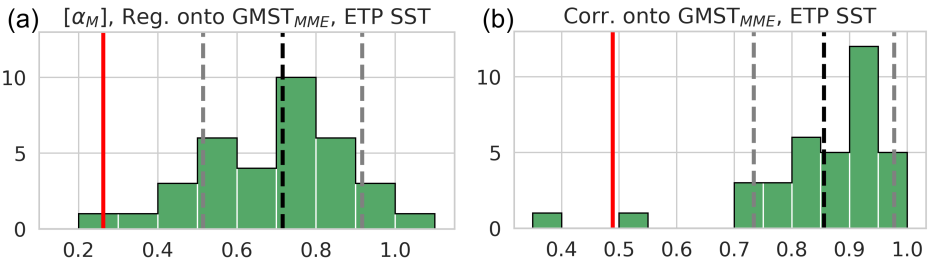

FIGURE 7 Histograms of (a) regression coefficients and (b) correlation coefficients of SST (in K) over the eastern tropical Pacific (180°–80°W, 10°S–10°N) onto the $GMST_{MME}$ (in K), derived from 36 multi-model members. Each panel shows the multi-model mean (black dashed vertical line), ±1σ range (grey dashed vertical line), and mean observed values (red solid vertical line) [Colour figure can be viewed at wileyonlinelibrary.com]

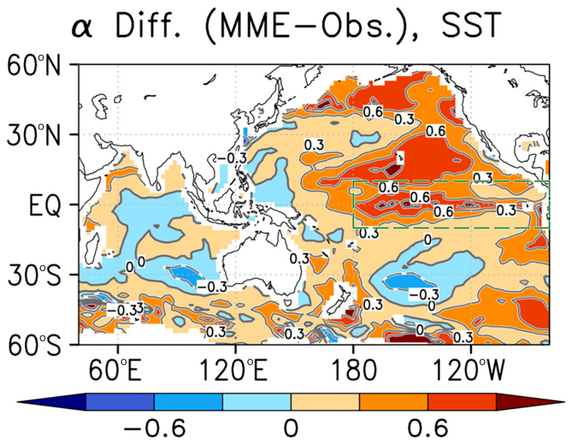

FIGURE 8 Differences in regression coefficients of SST (in K) onto GMST (in K) between the MME obtained from 36 historical simulations and the average of the observed records (MME minus the observed records). The box (dashed line) encloses the eastern tropical Pacific (180°–80°W, 10°S–10°N) [Colour figure can be viewed at wileyonlinelibrary.com]

TABLE 9 Temporal variances of SST over the eastern TP (180°–80°W, 10°S–10°N) obtained from multi-model historical simulations and the observed records

	Obs.	Model
Non-extracted	0.030	0.062 ± 0.031
EFC	0.008	0.052 ± 0.028
ICV	0.022	0.013 ± 0.010
ICV/EFC	2.792	0.371 ± 0.432

Note: Listed are the temporal variances in the non-extracted anomalies (row 2), EFCs estimated by Method I (row 3), and ICVs estimated by Method I (row 3). The bottom row gives the ratios of the EFC to ICV variances. The errors in the right column are the standard deviations among the multi-model members.

in the eastern equatorial Pacific might inhibit surface warming associated with anthropogenic forcing (Clement *et al*., 1996) in the observed records, but such an ocean thermostat mechanism is not always represented in simulations. As pointed out by Seager *et al*. (2019), when the relative humidity and wind speed over the ETP in the mean states of the CMIP5 models are excessively high and low, respectively, the local SST sensitivity to the radiative forcing is overestimated. Misrepresenting either the regional response of the external forcing or the ocean–atmosphere ICV in a climate model will lead to over-/under-estimations of the other. Therefore, to improve climate models, appropriate evaluations of the EFC and ICV based on the isolating methods (such as Method I) are necessary. Furthermore, the poor representation of the ICV in historical simulations still keeps an importance of the climate research based on the observed records as well as proxy climate data.

5 | SUMMARY

Applying three statistical procedures, we isolated the decadal ICV and the EFC from observed SST and SLP records over the Indo-Pacific sector during the 1958–2017 period. In Method I, the EFC is represented by the $GMST_{MME}$ in historical simulations because the ICV must be negligible when the $GMST_{MME}$ is derived from sufficiently many ensemble members. The regressed anomalies of each variable at each grid point onto the $GMST_{MME}$ are regarded as the EFCs. After removing these regressed anomalies, the remaining anomalies are regarded as the ICVs. Method II is the conventional detrending method that removes the linear trend on each variable at each grid point. In Method III, the time series of the MME of each variable is calculated at each grid point based on selected simulations, and the time series is removed from the observed records at the same grid points. In an EOF analysis of the remaining anomalies obtained by the three methods, we demonstrated that in the most appropriate method, the leading EOFs and their associated PCs represent the background physics of the large-scale air–sea interactions in any analysis domain. Although the remaining

SST and SLP anomalies were statistically independent, the decadal time series of the leading EOFs of those anomalies were significantly correlated in Method I. However, an EOF analysis of the remaining anomalies by Methods II and III often yielded peculiar appearances in the spatial patterns and time series, which were attributable to over- or under-removal of the EFC. Therefore, among the tested methods, we conclude that Method I best extracts the decadal ICV from the observed SST and SLP records over the Indo-Pacific sector.

By applying Method I to 36 individual historical simulations, we evaluated the reproducibilities of both the decadal ICV and the EFC. Most of the climate models artificially enhance the EFC and reduce the ICV when simulating SST over the ETP, where a centre of active ICV appears in the observed SST records.

Instead of the three methods in evaluating the local EFCs, we may introduce an alternative method by regressing the observed anomalies of a certain variable at the individual grid points onto the MME of SAT at the same grid point. This method is basically similar to the Method I, while the $GMST_{MME}$ is replaced by the MME of local SAT in this method. However, we are not ready for this alternative method because the MME at the local grid point based only 36 ensemble members still fails to represent the EFCs in local SAT/SST, as discussed in section 3. Recently, the large ensemble simulations such as >100 members for a single model (Watanabe *et al.*, 2021) become available. Further research with large ensembles is desired to re-evaluate the EFCs in the MME of local SAT or SST.

For accurate decadal climate predictions, we must understand the background mechanisms of the ICV and the effect of external forcing, and properly express these effects in climate models. By clarifying the importance of isolating the ICV and EFC in each climate variable on each region, we expect to stimulate further investigations of the mechanism underlying the decadal ICV and evaluations of climate model performances, thereby improving future climate projections over decades and centuries.

ACKNOWLEDGEMENTS

We thank two anonymous reviewers for their thoughtful and constructive comments on an earlier version of this manuscript. The Japan Society for the Promotion of Science partly supported this work with a Grants-in-Aid for Scientific Research (KAKENHI) (Grant Nos. JP18H03726, JP19H05702 and JP20K04072).

FUNDING INFORMATION

Japan Society for the Promotion of Science, Grant Number: JP18H03726, JP19H05702 and JP20K04072.

CONFLICT OF INTEREST

The authors declare no potential conflict of interest.

ORCID

Yuma Miyaji https://orcid.org/0000-0002-8446-6523

REFERENCES

Alexander, M.A., Bladé, I., Newman, M., Lanzante, J.R., Lau, N.-C. and Scott, J.D. (2002) The atmospheric bridge: the influence of ENSO teleconnections on air–sea interaction over the global oceans. *Journal of Climate*, 15, 2205–2231.

Bjerknes, J. (1969) Atmospheric teleconnections from the equatorial Pacific. *Monthly Weather Review*, 97, 163–172.

Bordbar, M.H., Martin, T., Latif, M. and Park, W. (2017) Role of internal variability in recent decadal to multidecadal tropical Pacific climate changes. *Geophysical Research Letters*, 44, 4246–4255.

Chen, X. and Tung, K.K. (2014) Varying planetary heat sink led to global-warming slowdown and acceleration. *Science*, 345, 897–903.

Chikamoto, Y., Timmermann, A., Luo, J.J., Mochizuki, T., Kimoto, M., Watanabe, M., Ishii, M., Xie, S.P. and Jin, F.F. (2015) Skilful multi-year predictions of tropical trans-basin climate variability. *Nature Communications*, 6, 6869.

Clement, A.-C., Seager, R., Cane, M.-A. and Zebiak, S.-E. (1996) An ocean dynamical thermostat. *Journal of Climate*, 9, 2190–2219.

Coats, S. and Karnauskas, K.B. (2017) Are simulated and observed twentieth century tropical Pacific sea surface temperature trends significant relative to internal variability? *Geophysical Research Letters*, 44, 9928–9937.

Dai, A., Fyfe, J.C., Xie, S.-P. and Dai, X. (2015) Decadal modulation of global surface temperature by internal climate variability. *Nature Climate Change*, 5, 555–559.

Dee, D.P., Uppala, S.M., Simmons, A.J., Berrisford, P., Poli, P., Kobayashi, S., Andrae, U., Balmaseda, M.A., Balsamo, G., Bauer, P., Bechtold, P., Beljaars, A.C.M., van de Berg, L., Bidlot, J., Bormann, N., Delsol, C., Dragani, R., Fuentes, M., Geer, A.J., Haimberger, L., Healy, S.B., Hersbach, H., Hólm, E. V., Isaksen, L., Kållberg, P., Köhler, M., Matricardi, M., McNally, A.P., Monge-Sanz, B.M., Morcrette, J.-J., Park, B.-K., Peubey, C., de Rosnay, P., Tavolato, C., Thépaut, J.-N. and Vitart, F. (2011) The ERA-Interim reanalysis: configuration and performance of the data assimilation system. *Quarterly Journal of the Royal Meteorological Society*, 137, 553–597.

Deser, C. and Phillips, A.S. (2006) Simulation of the 1976/77 climate transition over the North Pacific: sensitivity to tropical forcing. *Journal of Climate*, 19, 6170–6180.

Dong, L. and Mcphaden, M.J. (2017) Why has the relationship between Indian and Pacific Ocean decadal variability changed in recent decades? *Journal of Climate*, 30, 1971–1983.

Du, Y. and Xie, S.-P. (2008) Role of atmospheric adjustments in the tropical Indian Ocean warming during the 20th century in climate models. *Geophysical Research Letters*, 35, L08712.

Easterling, D.R. and Wehner, M.F. (2009) Is the climate warming or cooling? *Geophysical Research Letters*, 36, L08706.

England, M.H., McGregor, S., Spence, P., Meehl, G.A., Timmermann, A., Cai, W., Gupta, A.S., McPhaden, M.J., Purich, A. and Santoso, A. (2014) Recent intensification of wind-driven circulation in the Pacific and the ongoing warming hiatus. *Nature Climate Change*, 4, 222–227.

Han, W., Meehl, G.A., Hu, A., Alexander, M.A., Yamagata, T., Yuan, D., Ishii, M., Pegion, P., Zheng, J., Hamlington, B.D., Quan, X.-W. and Leben, R.R. (2014b) Intensification of decadal and multi-decadal sea level variability in the western tropical Pacific during recent decades. *Climate Dynamics*, 43, 1357–1379.

Han, W., Vialard, J., Mcphaden, M.J., Lee, T., Masumoto, Y., Feng, M. and de Ruijter, W.P.M. (2014a) Indian Ocean decadal variability: a review. *Bulletin of the American Meteorological Society*, 95, 1679–1703.

Henley, B.J. (2017) Pacific decadal climate variability: indices, patterns and tropical-extratropical interactions. *Global and Planetary Change*, 155, 42–55.

Hegerl, G.C., Zwiers, F.W., Braconnot, P., Gillett, N.P., Luo, Y., Marengo Orsini, J.A., Nicholls, N., Penner, J.E. and Stott, P.A. (2007) Understanding and attributing climate change. In: Solomon, S., Qin, D., Manning, M., Chen, Z., Marquis, M., Averyt, K.B., Tignor M. and Miller H.L. (Eds.) *Climate Change 2007: The Physical Science Basis. Contribution of Working Group I to the Fourth Assessment Report of the Intergovernmental Panel on Climate Change*. Cambridge, England: Cambridge University Press.

Hirahara, S., Ishii, M. and Fukuda, Y. (2014) Centennial-scale sea surface temperature analysis and its uncertainty. *Journal of Climate*, 27, 57–75.

Kalnay, E., Kanamitsu, M., Kistler, R., Collins, W., Deaven, D., Gandin, L., Iredell, M., Saha, S., White, G., Woollen, J., Zhu, Y., Leetmaa, A., Reynolds, R., Chelliah, M., Ebisuzaki, W., Higgins, W., Janowiak, J., Mo, K.C., Ropelewski, C., Wang, J., Jenne, R. and Joseph, D. (1996) The NCEP/NCAR 40-year reanalysis project. *Bulletin of the American Meteorological Society*, 77, 437–471.

Kobayashi, S., Ota, Y., Harada, Y., Ebita, A., Moriya, M., Onoda, H., Onogi, K., Kamahori, H., Kobayashi, C., Endo, H., Miyaoka, K. and Takahashi, K. (2015) The JRA-55 reanalysis: general specifications and basic characteristics. *Journal of the Meteorological Society of Japan*, 93, 5–48.

Kosaka, Y. and Xie, S.P. (2013) Recent global-warming hiatus tied to equatorial Pacific surface cooling. *Nature*, 501, 403–407.

Kosaka, Y. and Xie, S.-P. (2016) The tropical Pacific as a key pacemaker of the variable rates of global warming. *Nature Geoscience*, 9, 669–673.

L'Heureux, M.L., Lee, S. and Lyon, B. (2013) Recent multidecadal strengthening of the Walker circulation across the tropical Pacific. *Nature Climate Change*, 3, 571–576.

Lee, S.-K., Park, W., Baringer, M.O., Gordon, A.L., Huber, B. and Liu, Y. (2015) Pacific origin of the abrupt increase in Indian Ocean heat content during the warming hiatus. *Nature Geoscience*, 8, 445–449.

Luo, J.J., Sasaki, W. and Masumoto, Y. (2012) Indian Ocean warming modulates Pacific climate change. *Proceedings of the National Academy of Sciences of the United States of America*, 109, 18701–18706.

Maher, N., England, M.H., Gupta, A.S. and Spence, P. (2018) Role of Pacific trade winds in driving ocean temperatures during the recent slowdown and projections under a wind trend reversal. *Climate Dynamics*, 51, 321–336.

Medhaug, I., Stolpe, M.B., Fischer, E.M. and Knutti, R. (2017) Reconciling controversies about the "global warming hiatus". *Nature*, 545, 41–47.

Meehl, G.A., Arblaster, J.M., Fasullo, J.T., Hu, A. and Trenberth, K. E. (2011) Model-based evidence of deep-ocean heat uptake during surface-temperature hiatus periods. *Nature Climate Change*, 1, 360–364.

Neeti, N. and Eastman, J.R. (2014) Novel approaches in extended principal component analysis to compare spatio-temporal patterns among multiple image time series. *Remote Sensing of Environment*, 148, 84–96.

Nitta, T. and Yamada, S. (1989) Recent warming of tropical sea surface temperature and its relationship to the Northern Hemisphere circulation. *Journal of the Meteorological Society of Japan*, 67, 375–383.

Power, S., Casey, T., Folland, C., Colman, A. and Mehta, V. (1999) Interdecadal modulation of the impact of ENSO on Australia. *Climate Dynamics*, 15, 319–324.

Rayner, N.A., Horton, E.B., Parker, D.E., Folland, C.K. and Hackett, R.B. (1996) *Version 2.2 of the global sea-ice and sea surface temperature data set, 1903–1994*. Bracknell: Hadley Centre, Met Office. Technical note 74.

Rayner, N.A., Parker, D.E., Horton, E.B., Folland, C.K., Alexander, L.V., Rowell, D.P., Kent, E.C. and Kaplan, A. (2003) Global analyses of sea surface temperature, sea ice, and night marine air temperature since the late nineteenth century. *Journal of Geophysical Research*, 108, 4407.

Reynolds, R.W., Smith, T.M., Liu, C., Chelton, D.B., Casey, K.S. and Schlax, M.G. (2007) Daily high-resolution-blended analyses for sea surface temperature. *Journal of Climate*, 20, 5473–5496.

Seager, R., Cane, M., Henderson, N., Lee, D.-E., Abernathey, R. and Zhang, H. (2019) Strengthening tropical Pacific zonal sea surface temperature gradient consistent with rising greenhouse gases. *Nature Climate Change*, 9, 517–522.

Shakun, J.D. and Shaman, J. (2009) Tropical origins of North and South Pacific decadal variability. *Geophysical Research Letters*, 36, L19711.

Tanimoto, Y., Iwasaka, N. and Hanawa, K. (1997) Relationships between sea surface temperature, the atmospheric circulation and air–sea fluxes on multiple time scales. *Journal of the Meteorological Society of Japan*, 75, 831–849.

Taylor, K.E., Stouffer, R.J. and Meehl, G.A. (2012) An overview of CMIP5 and the experiment design. *Bulletin of the American Meteorological Society*, 93, 485–498.

Tokinaga, H., Xie, S.P., Deser, C., Kosaka, Y. and Okumura, Y.M. (2012) Slowdown of the Walker circulation driven by tropical Indo-Pacific warming. *Nature*, 491, 439–443.

Trenberth, K.E. and Hurrell, J.W. (1994) Decadal atmosphere–ocean variations in the Pacific. *Climate Dynamics*, 9, 303–319.

Uppala, S.M., KÅllberg, P.W., Simmons, A.J., Andrae, U., Bechtold, V.D.C., Fiorino, M., Gibson, J.K., Haseler, J., Hernandez, A., Kelly, G.A., Li, X., Onogi, K., Saarinen, S., Sokka, N., Allan, R.P., Andersson, E., Arpe, K., Balmaseda, M.A., Beljaars, A.C.M., Berg, L.V.D., Bidlot, J., Bormann, N., Caires, S., Chevallier, F., Dethof, A., Dragosavac, M., Fisher, M., Fuentes, M., Hagemann, S., Hólm, E., Hoskins, B.J., Isaksen, L., Janssen, P.A.E.M., Jenne, R., Mcnally, A.P., Mahfouf, J.F., Morcrette, J.J., Rayner, N.A., Saunders, R.W., Simon, P., Sterl, A., Trenberth, K.E., Untch, A., Vasiljevic, D., Viterbo, P. and Woollen, J. (2005) The ERA-40 re-analysis. *Quarterly Journal of the Royal Meteorological Society*, 131, 2961–3012.

Watanabe, M., Dufresne, J.-L., Kosaka, Y., Mauritsen T.and, Tatebe, H, 2021: Enhanced warming constrained by past trends in equatorial Pacific Sea surface temperature gradient. *Nature Climate Change*, 11, 33–37.

Xu, Y. and Hu, A. (2018) How would the 21st-century warming influence Pacific decadal variability and its connection to North American rainfall: assessment based on a revised procedure for IPO/PDO. *Journal of Climate*, 31, 1547–1563.

Yasunaka, S. and Hanawa, K. (2011) Intercomparison of historical sea surface temperature datasets. *International Journal of Climatology*, 31, 1056–1073.

Zhang, X., Liang, S., Wang, G., Yao, Y., Jiang, B. and Cheng, J. (2016) Evaluation of the reanalysis surface incident shortwave radiation products from NCEP, ECMWF, GSFC, and JMA using satellite and surface observations. *Remote Sensing*, 8, 225.

How to cite this article: Miyaji, Y., Hasegawa, T., & Tanimoto, Y. (2023). Intercomparisons of methods for extracting the internal climate variability from the observed records over the Indo-Pacific sector. *International Journal of Climatology*, *43*(1), 57–75. https://doi.org/10.1002/joc.7729